FEBS Letters

FEBS PRESS science publishing by scientists

RESEARCH ARTICLE

Mapping the sclerostin–LRP4 binding interface identifies critical interaction hotspots in loops 1 and 3 of sclerostin

Svetlana Katchkovsky[1], Reut Meiri[2], Shiran Lacham-Hartman[3], Yaron Orenstein[2,4], Noam Levaot[1] and Niv Papo[3]

1 Department of Physiology and Cell Biology, Faculty of Health Sciences, Ben-Gurion University of the Negev, Beer-Sheva, Israel
2 Department of Computer Science, Bar-Ilan University, Ramat Gan, Israel
3 Avram and Stella Goldstein-Goren Department of Biotechnology Engineering and the National Institute of Biotechnology in the Negev, Ben-Gurion University of the Negev, Beer-Sheva, Israel
4 The Mina and Everard Goodman Faculty of Life Sciences, Bar-Ilan University, Ramat Gan, Israel

Correspondence
N. Papo, Avram and Stella Goldstein-Goren Department of Biotechnology Engineering, Ben-Gurion University of the Negev, P.O. Box 653, Beer-Sheva 8410501, Israel
Tel: +972502029729
E-mail: papo@bgu.ac.il

(Received 3 July 2024, revised 19 August 2024, accepted 21 September 2024)

doi:10.1002/1873-3468.15033

Edited by Christian Griesinger

The interaction of sclerostin (Scl) with the low-density lipoprotein receptor-related protein 4 (LRP4) leads to a marked reduction in bone formation by inhibiting the Wnt/β-catenin pathway. To characterize the Scl–LRP4 binding interface, we sorted a combinatorial library of Scl variants and isolated variants with reduced affinity to LRP4. We identified Scl single-mutation variants enriched during the sorting process and verified their reduction in affinity toward LRP4—a reduction that was not a result of changes in the variants' secondary structure or stability. We found that Scl positions K75 (loop 1) and V136 (loop 3) are critical hotspots for binding to LRP4. Our findings establish the foundation for targeting these hotspots for developing novel therapeutic strategies to promote bone formation.

Keywords: deep mutational scanning; epitope mapping; LRP4; Sclerostin; Wnt/β-catenin pathway; yeast surface display

Proper functioning of the Wnt/β-catenin signaling pathway is crucial for the maintenance of bone integrity [1,2]. One of the major antagonists of this pathway is sclerostin (Scl), a soluble glycosylated protein produced mainly by osteocytes, the most abundant cells in bone tissue [3,4]. The inhibitory activity of Scl is manifested in a reduction in osteoblast differentiation, proliferation, maturation, and mineralization, leading to a substantial reduction in bone formation [5,6]. Scl inhibits the Wnt pathway by binding directly to several members of the low-density lipoprotein receptor-related protein family of transmembrane receptors (LRPs), namely, LRP4, and LRP5 and LRP6 (designated LRP5/6) [7–9]. It has been shown that LRP4 anchors Scl to bone and facilitates Scl-LRP5/6 binding, resulting in enhanced inhibition of the Wnt pathway [7,9–13]. Similarly, our previous study indicated that inhibition of the Wnt pathway by Scl depends on its prior binding to LRP4, which putatively promotes an orientation of Scl that facilitates its subsequent binding to LRP6 [14].

Although the extracellular domain organization of LRP4 differs from that of LRP5/6, the three receptors share several structural features, including four six-bladed β-propeller domains (i.e., E1, E2, E3, and E4) [9,15–18]. Extensive studies on Scl, LRP5/6, and their interactions have shown that the core of Scl comprises a cystine knot with three loops [19], where loops 1 and 3 form rigid β-sheet structures, whereas loop 2 is relatively flexible and unstructured and faces away

Abbreviations
CD, circular dichroism; DSC, differential scanning calorimetry; FACS, fluorescence-activated cell sorting; HBM, high bone mass; LRP4, low-density lipoprotein receptor-related protein 4; PBSA 1%, phosphate-buffered saline with 1% bovine serum albumin; PPI, protein–protein interaction; Scl, sclerostin; SPR, surface plasmon resonance; WT, wild-type; YSD, yeast surface display.

from loops 1 and 3. It is also known that the N- and C-terminal arms of Scl are disordered and highly flexible [19]. Finally, high-resolution crystal structures of the LRP6 E1E2–Scl complex have revealed that the interaction between Scl and E1 of LRP6 is mediated through loop 2 of Scl, whereas E2 of LRP6 binds to the C-terminal arm of Scl [20–22].

Much less is known about the LRP4–Scl binding interaction. However, it has been suggested that the binding of Scl to LRP5/6 and LRP4 is mediated by different Scl epitopes [23]. Furthermore, it is known that mutations in Scl and LRP4 are pathogenic, causing a rare high bone mass (HBM) condition in humans, known as sclerosteosis 1 (for mutations in Scl) [24–27] or sclerosteosis 2 (for mutations in LRP4) [11,28], as a result of less efficient inhibition of the Wnt pathway by Scl. HBM mutations located in the E3 β-propeller of LRP4 impair the LRP4–Scl interaction, suggesting that LRP4–Scl binding is mediated through the E3 domain [10,11]. More recently, a novel HBM-causing mutation in the E1 domain of LRP4 was shown to reduce the inhibitory activity of Scl on the Wnt pathway [29], suggesting that the E1 domain may participate in the LRP4–Scl interaction.

Our recent work showed the LRP4–Scl interaction to be crucial for inhibition of the Wnt pathway by Scl [14]. Furthermore, this interaction was competitively disrupted by an Scl protein with a point mutation, that is, Scl_{N93A}, which shares a common binding site with Scl on LRP4. Furthermore, we showed that 2 weeks of biweekly injections with the Scl_{N93A} variant resulted in a significant increase in the rate of bone formation and bone volumetric parameters in developing mice [14]. These findings suggest that disruption of the LRP4–Scl binding interface enables undisturbed bone formation by promoting Wnt signaling. Therefore, it appears that the LRP4–Scl interaction can be leveraged for advancing the development of novel therapeutics for the treatment of various bone disorders. Importantly, identifying the Scl interaction site with LRP4 is pivotal for targeting this interaction.

Elucidating the LRP4–Scl binding interface by conventional structural methods, such as crystallography, poses a particular challenge. Specifically, it is difficult to prepare large quantities of correctly folded full-length LRP4 or its specific domains, which is a prerequisite for crystallography [30]. Another commonly used approach for elucidating receptor-ligand binding epitopes is alanine scanning, where individual amino acids in the protein of interest are systematically substituted for alanine [31,32]. This method also has drawbacks in that it requires the purification and binding affinity measurement for each variant, making it challenging and time-consuming.

We therefore opted to utilize an epitope mapping technique using a yeast surface display (YSD) affinity screen of an Scl library predominantly having a single mutation (to any amino acid) per variant. Epitope mapping, which is widely used to study protein–protein interactions (PPIs) [33–35], assumes that protein variants with mutations in positions located within the binding interface will result in a change in binding affinity to the target protein. The major advantage of this approach is that there is no need to purify the proteins and test each one of them separately to evaluate their binding properties, since protein variants with correct folding and reduced binding to the target can easily be detected by fluorescence-activated cell sorting (FACS). Further integration of high-throughput sequencing of the screened library and comprehensive bioinformatic analysis of the frequency and enrichment of each variant allows the identification of mutations to amino acids other than alanine, which enables the identification of hotspots, that is, positions where the residues make a major contribution to the protein–protein binding free energy [36–40].

Here, following YSD display of a combinatorial library of Scl variants, we screened the library for binding to soluble LRP4 and isolated a fraction of low-affinity binders by using flow cytometry. Thereafter, we screened the low-affinity fraction for binding to soluble LRP5/6 to minimize the instances of Scl variants with reduced affinity to LRP4 due to incorrect folding on the yeast surface. Through this process, screening for Scl binders with both low affinity to LRP4 and high affinity to LRP5/6 has been successfully achieved, since distinct epitopes in Scl are involved in binding to LRP5/6 and LRP4. Thereafter, by employing high-throughput sequencing and bioinformatic analysis of the sequencing data, we obtained a library enriched with Scl variants having a single mutation and reduced binding to LRP4. We then tested these variants for binding to soluble LRP4 by using YSD and surface plasmon resonance (SPR). To make sure that the reduction in affinity of each variant relative to the wild-type (WT) Scl (Scl_{WT}) was not the result of a decrease in stability or incorrect folding, we also tested these variants for thermal stability [by differential scanning calorimetry (DSC)] and determined their secondary structure [by circular dichroism (CD)]. This methodology enabled us to pinpoint two positions in Scl that are hotspots for the binding of Scl to LRP4, namely, position K75 in loop 1 and V136 in loop 3 of Scl, which are expected to be in direct contact with LRP4. These findings contribute to better

understanding of how the Wnt pathway can be manipulated to treat various skeletal diseases and restore bone health.

Methods

Combinatorial library of Scl single-mutation variants: construction and fractional sorting

An Scl (UniProt [41] primary accession number Q9BQB4, residues Gln24-Tyr213) library with a low mutation frequency (1–4 base substitutions per clone) was generated in a pCTCON expression vector by GenScript (Piscataway, NJ, USA). The library was transformed into a competent *Saccharomyces cerevisiae* EBY100 yeast strain (a gift from Amir Aharoni, Ben-Gurion University of the Negev) by electroporation using a MicroPulser electroporator (Bio-Rad, Hercules, CA, USA), as previously described [35]. The transformed yeast cells were grown overnight at 30 °C with shaking at 300 rpm in SDCAA selective medium (2% dextrose, 0.67% yeast nitrogen base, 0.5% Bacto™ Casamino Acids, 1.47% sodium citrate, and 0.429% citric acid monohydrate, adjusted to pH 4.5) to an OD_{600} of 10 (10^8 cells·mL^{-1}). A library size of 1.2×10^6 transformants was verified by plating serial dilutions on SDCAA plates (2% dextrose, 0.67% yeast nitrogen base, 0.5% Bacto Casamino Acids, 1.54% Na_2HPO_4, 1.856% $NaH_2PO_4{\cdot}H_2O$, 18.2% sorbitol, and 1.5% agar). Library expression was induced by incubating the transformed cells with SGCAA medium (2% galactose, 0.67% yeast nitrogen base, 0.5% Bacto Casamino Acids, 1.47% sodium citrate, and 0.429% citric acid monohydrate) overnight at 30 °C with shaking at 300 rpm to an OD_{600} of 5. Library expression was detected on the surface of the yeast cells by incubating the cells with 1 : 50 mouse anti-c-Myc antibody 9E10 for 1 h at room temperature, followed by incubation with 1 : 50 anti-mouse IgG (whole molecule)-R-phycoerythrin antibody produced in goat (Sigma-Aldrich) for 20 min on ice. Labeled cells (30 000 per experimental condition) were analyzed on a FACSCanto II flow cytometer (BD Biosciences, Franklin Lakes, NJ, USA). Data analysis was performed using FLOWJO software (BD, Ashland, OR, USA). For library sorting, the cells were incubated with 5 nM soluble His-tagged human LRP4 or 650 nM soluble His-tagged mouse LRP6 (R&D Systems, Minneapolis, MN, USA) and 1 : 100 affinity-purified chicken anti-c-Myc antibody (Immunology Consultants Laboratory, Inc., Portland, OR, USA) for 1 h at room temperature, followed by double staining with a 1 : 50 FITC-conjugated anti-6 × His-tag monoclonal antibody (Invitrogen, Waltham, MA, USA) and 1 : 50 Alexa Fluor™ 555-labeled goat anti-chicken IgY (H + L) antibody (Invitrogen) for 20 min in the dark on ice. The desired populations were collected on an iCyt Synergy FACS apparatus (Sony Biotechnology, San Jose, CA, USA) and allowed to recover at 30 °C with shaking at 300 rpm in SDCAA medium until the culture reached an OD_{600} of 8. All proteins and antibodies were diluted to working concentrations in phosphate-buffered saline with 1% bovine serum albumin (designated PBSA 1%), and all wash steps were performed with PBSA 1%.

High-throughput sequencing of the fractionated library

The plasmid DNA of the parental presorted library and the two affinity-sorted library fractions (each yielding ~ 10^8 yeast cells) were individually extracted by using the E.Z.N.A. Yeast Plasmid Mini Kit (Omega Bio-Tek, Norcross, GA, USA) according to the manufacturer's protocol. The kit products were run on a 1% agarose gel and then purified with a HiYield Gel/PCR Fragments Extraction Kit (RBC Bioscience, New Taipei City, Taiwan). Due to the low mutation frequency of the libraries (1–4 base substitutions per amplicon), amplicons were expected to consist primarily of sequences with a single mutation, that is, amplicons with very low complexity. Therefore, to prevent the depletion of fluorescently labeled deoxyribonucleotide triphosphates (dNTPs) during each cycle of the high-throughput sequencing, it was necessary to introduce sequence complexity. To this end, we designed Scl-specific primers with heterogeneity spacers (N, NN, and NNN), that is, mixed-sequence bases. Consequently, the amplicons in each library exhibited variable lengths (+0–3 bp), ensuring an even distribution of all four bases for each sequencing cycle.

The following Scl-specific primers were used:

Forward overhang primers:

1 5′TCGTCGGCAGCGTCAGATGTGTATAAGAGACAGCAAGGGTGGCAAGCGTTTAAAAATGACGC

2 5′TCGTCGGCAGCGTCAGATGTGTATAAGAGACAGNCAAGGGTGGCAAGCGTTTAAAAATGACGC

3 5′TCGTCGGCAGCGTCAGATGTGTATAAGAGACAGNNCAAGGGTGGCAAGCGTTTAAAAATGACGC

4 5′TCGTCGGCAGCGTCAGATGTGTATAAGAGACAGNNNCAAGGGTGGCAAGCGTTTAAAAATGACGC

Reverse overhang primers:

5 5′GTCTCGTGGGCTCGGAGATGTGTATAAGAGACAGGTACGCGTTCTCTAATTCGGCTTGGTTAGCT

6 5′GTCTCGTGGGCTCGGAGATGTGTATAAGAGACAGNGTACGCGTTCTCTAATTCGGCTTGGTTAGCT

7 5′GTCTCGTGGGCTCGGAGATGTGTATAAGAGACAGNNGTACGCGTTCTCTAATTCGGCTTGGTTAGCT

8 5′GTCTCGTGGGCTCGGAGATGTGTATAAGAGACAGNNNGTACGCGTTCTCTAATTCGGCTTGGTTAGCT

Black letters represent the overhang adapter sequence, green letters represent the heterogeneity spacers, and blue letters represent the Scl-specific sequence.

Thereafter, 12.5 ng of plasmid DNA per library was amplified using 2× KAPA HiFi HotStart ReadyMix (Kapa Biosystems, Wilmington, MA, USA). The PCR conditions were as follows: 95 °C for 3 min, followed by 25 cycles of 95 °C for 30 s, 64 °C for 30 s, 72 °C for 30 s, and a final extension at 72 °C for 5 min. For index PCR, library DNA was amplified with Forward Nextera XT Index 1 Primers (N701, N702, and N703) and the Reverse Nextera XT Index 2 Primer (S517) using 2× KAPA HiFi HotStart ReadyMix. The PCR conditions were as follows: 95 °C for 3 min, followed by 8 cycles of 95 °C for 30 s, 64 °C for 30 s, 72 °C for 30 s, and a final extension at 72 °C for 5 min. After each PCR reaction, the DNA was purified using AMPure XP beads (Omega Bio-Tek, Inc.). The size of the PCR products was validated by running the products on a Bioanalyzer DNA 1000 chip. The products were quantified using a Qubit™ DNA high-sensitivity assay kit. The sequencing was performed by the NGS department of Hy Laboratories (Hylabs, Rehovot, Israel) on an Illumina Miseq using the MiSeq Reagent Kit v3 (600 cycles) (Illumina, San Diego, CA, USA).

Quality filtration and integration of the high-throughput sequencing data

Sequencing data from each library were treated identically. An average Illumina quality score was calculated for each read in a given set of paired-end reads. Read pairs with an average quality score of < 20 (i.e., the probability that the corresponding base identification is incorrect is $> 1/100$) were discarded. The remaining reads were merged into a single sequence by the following steps: (a) matching of the forward and reverse sequences using the Illumina ID; (b) identifying the start and end positions of each protein sequence within the full sequence by locating the first and last two codons, respectively, for the forward and reverse sequencing data, while accepting all possible single-nucleotide changes; (c) converting the reverse DNA sequences into their reverse-complement counterparts; and (d) merging the forward and reverse sequences by finding an alignment that contains the smallest number of mismatches between the pair. In cases of mismatches, the codon with the highest read quality was selected for the final merged sequence.

Computational analysis of the high-throughput sequencing data

The DNA sequences of the parental presorted library (designated $\mathrm{Scl_{NAIVE}}$) and the two affinity-sorted library fractions (designated $\mathrm{LRP4_{LOW}}$, and $\mathrm{LRP4_{LOW}LRP6}$) were translated to their respective amino acid sequences. Sequences that contained a premature stop codon caused by mutagenesis were filtered out. Thereafter, sequences containing more than one mutation were filtered out. For each sequence variant with a single mutation, the number of occurrences in each library was counted. Since the total read count varied across libraries, the frequency of variant mut_i in library *lib* ($f_{\mathrm{mut}_i\ lib}$) was calculated using the following equation:

$$f_{\mathrm{mut}_i\ lib} = \frac{\#\text{reads mut}_i\ lib}{\sum_{j=1}^{n} \#\text{reads mut}_j\ lib} \quad (1)$$

where $\#\text{reads mut}_i\ lib$ is the number of reads of a variant mut_i in library *lib* and $\sum_{j=1}^{n}\#\text{reads mut}_j\ lib$ is the sum of all the reads for all variants in library *lib*. This normalization prevents the bias resulting from differences in the number of reads in each library.

Next, to compare the frequency of each variant to that of the WT in the same library, a normalized frequency (NF) was defined:

$$NF_{mut_i lib} = \frac{f_{\mathrm{mut}_i\ lib}}{f_{\mathrm{WT}\ lib}} \quad (2)$$

which is the ratio between the frequency of a given variant mut_i in library *lib* and the frequency of the WT clone within library *lib*.

Based on the NFs, we calculated enrichment ratios (ERs) for each variant:

$$\mathrm{ER}_{mut_i\ \text{LRP4 low affinity}_{\mathrm{LIB}}} = \frac{\mathrm{NF}_{\mathrm{mut}_i\ LRP4_{LOW}}}{\mathrm{NF}_{\mathrm{mut}_i\ Scl_{NAIVE}}}$$

$$\mathrm{ER}_{mut_i\ \text{LRP6 binders}_{\mathrm{LIB}}} = \frac{\mathrm{NF}_{\mathrm{mut}_i\ LRP4_{LOW}LRP6}}{\mathrm{NF}_{\mathrm{mut}_i\ Scl_{NAIVE}}}$$

$$\mathrm{ER}_{mut_i\ \text{LRP6 binders vs LRP4 low affinity}_{\mathrm{LIB}}} = \frac{\mathrm{NF}_{\mathrm{mut}_i\ LRP4_{LOW}LRP6}}{\mathrm{NF}_{\mathrm{mut}_i\ LRP4_{LOW}}} \quad (3)$$

where $\mathrm{NF}_{\mathrm{mut}_i lib}$ is the NF of a variant mut_i in library *lib*.

The statistical significance of the ERs was determined by using a two-sided Poisson exact test to calculate a *P*-value for the enrichment of each variant [42]. The Benjamini–Hochberg false discovery rate (FDR) was applied for multi-test correction [43].

Binding analysis for Scl single-mutation variants expressed on the yeast cell surface

cDNA sequences encoding for Scl single-mutation variants (residues Gln24-Tyr213 with a point mutation) were synthesized by Gene Universal Inc. (Newark, DE, USA). The sequences were subcloned into a YSD pCTCON vector in our laboratories and transformed into a competent *S. cerevisiae* EBY100 strain by electroporation. To detect the expression of the displayed protein variants, transformed

cells were incubated with a 1 : 100 affinity-purified chicken anti-c-Myc antibody for 1 h at room temperature, followed by a 1 : 50 Alexa Fluor 555-labeled goat anti-chicken IgY (H + L) antibody. For binding analysis of the displayed Scl variants, cells were incubated with different concentrations of soluble His-tagged human LRP4 (1, 10, and 50 nM) for 1 h at room temperature, followed by detection with a 1 : 50 FITC-conjugated anti-6 × His-tag monoclonal antibody (Invitrogen). All proteins and antibodies were diluted with PBSA 1%, and all wash steps were performed with PBSA 1%. Labelled cells (30 000 per experimental condition) were analyzed in an FACSCanto II flow cytometer (BD Biosciences). All experiments were repeated at least three times. Further FACS analysis was performed using FLOWJO software. All values were normalized, first to the respective yeast surface-displayed protein expression and then to the binding signal of Scl_{WT} at the relevant LRP4 concentration.

Protein purification

The following nomenclature is used for Scl single-mutation variants: Scl_{T11A}–Thr11Ala substitution, Scl_{E59G}–Glu59Gly substitution, Scl_{A74E}–Ala74Glu substitution, Scl_{K75E}–Lys75-Glu substitution, Scl_{K75Q}–Lys75Gln substitution, Scl_{K135R}–Lys135Arg substitution, and Scl_{V136D}–Val136Asp substitution.

To express the Scl_{WT} and Scl single-mutation variants in yeast, the sequences were amplified from the pCTCON template vector, while adding recognition sites for AvrII and ECORI restriction enzymes (NEB) by using 5′-ACA AAG AAT TCC GTC AAG GGT GGC AAG CGT3′ as the forward primer and 5′-AAA ACC TAG GGT ACG CGT TCT CTA ATT CGG-3′ as the reverse primer. The amplified gene sequences and pPICK9K plasmid (Invitrogen) were digested with AvrII and ECORI (NEB), ligated using Quick Ligase (NEB), and transformed into competent *Escherichia coli* cells by heat shock. Thereafter, the plasmids were transformed into electrocompetent *Pichia pastoris* GS115 strain cells, as previously described [44].

The highest-expressing clones (based on SDS/PAGE analysis of 6–9 clones per protein variant) were chosen for the subsequent large-scale production. Protein purification was scaled up as described previously [14]. Protein-containing fractions were pooled after determining relevant fractions by SDS/PAGE analysis, using staining with InstantBlue Coomassie protein stain (Abcam, Cambridge, UK). Protein concentrations were determined using a NanoDrop spectrophotometer (Thermo Fisher Scientific, Waltham, MA, USA), based on protein absorbance at 280 nm (percent extinction coefficient for Scl_{WT}, Scl_{K75E}, and $Scl_{K75Q} = 11.16$, for $Scl_{T11A} = 11.18$, and for $Scl_{V136D} = 11.15$). Protein yields were 2.6 $mg{\cdot}L^{-1}$ of starting yeast culture for Scl_{WT}, 2 $mg{\cdot}L^{-1}$ for Scl_{T11A}, 2.6 $mg{\cdot}L^{-1}$ for Scl_{K75E}, 4.4 $mg{\cdot}L^{-1}$ for Scl_{K75Q}, and 3.5 $mg{\cdot}L^{-1}$ for Scl_{V136D}. Following purification, a small fraction of each protein variant was treated with Endo Hf endoglycosidase (NEB, Ipswich, MA, USA), according to the manufacturer's protocol, to remove N-linked glycosylation.

Differential scanning calorimetry

DSC was performed with a Nano DSC differential scanning calorimeter (TA Instruments, New Castle, DE, USA). All proteins used in this assay were diluted to a concentration of 16.67 μM (0.5 $mg{\cdot}mL^{-1}$) with HEPES-buffered saline (10 mM HEPES, 150 mM NaCl). This buffer was also used for instrumental baseline scans. The protein solution was heated from 20 to 80 °C at a rate of 1 $°C{\cdot}min^{-1}$. The thermograms were normalized to the protein concentration and corrected for the instrument baseline. The data were analyzed using the NANOANALYZE software (TA Instruments) and fitted using a Gaussian two-peak model.

Circular dichroism spectroscopy

The proteins were diluted to 0.2 $mg{\cdot}mL^{-1}$ with an assay buffer (1 mM HEPES, 15 mM NaCl), and samples were scanned using a Jasco J-715 spectropolarimeter (Jasco, Kyoto, Japan). The appropriate high-tension voltage (< 600 V) was maintained during the measurements, which were conducted at 25 °C. The spectrum of each sample was recorded in a range of 200–260 nm using a quartz cuvette with a path length of 0.1 cm. The scanning speed was set to 50 $nm{\cdot}min^{-1}$ with a data collection interval of 0.5 nm. Background correction was performed using the assay buffer.

Surface plasmon resonance

Binding of the soluble purified Scl_{WT} protein and the Scl_{K75E}, Scl_{K75Q}, and Scl_{V136D} variants to recombinant human LRP4 (R&D Systems) was determined using a ProteOn XPR36 (Bio-Rad). Recombinant human LRP4 was immobilized on the surface of a XanTec SC HC200M 1022.a sensor chip (XanTec Bioanalytics GmbH, Duesseldorf, Germany) coated with a medium charge density polycarboxylate hydrogel. For the analysis of purified soluble Scl_{WT}, Scl_{K75Q}, and Scl_{V136D} binding, 3 or 6 μg of recombinant human LRP4 or 3 μg of bovine serum albumin (BSA) as a negative control were covalently attached to the surface of the chip in a 10 mM sodium acetate buffer, pH 4.0. This resulted in 3148, 6840, and 3302 response units (RU) for LRP4 and BSA, respectively. For the analysis of purified Scl_{K75E} binding, 3 μg of recombinant human LRP4 or 3 μg of BSA were covalently attached to the chip, as described above, to give 1679 and 1765 RU, respectively. Unbound esters were deactivated with 1 M ethanolamine HCl at pH 8.5.

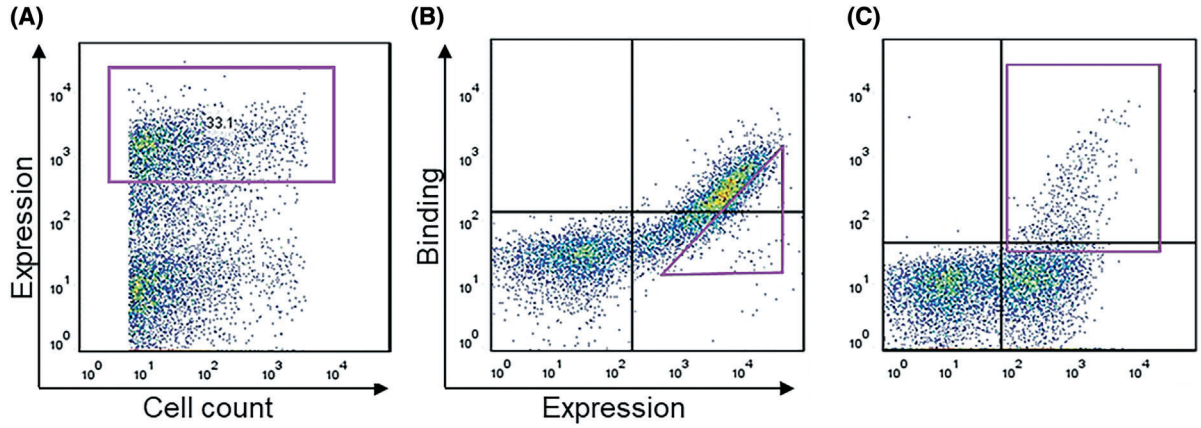

Fig. 1. Flow cytometry sorting of the combinatorial Scl library. (A) Library expression was monitored by staining with a phycoerythrin-conjugated antibody binding to a primary anti-c-Myc antibody. The purple rectangle gate indicates cells with the highest expression. (B) The library was incubated with 5 nM LRP4, and the low-affinity library fraction was collected (purple triangle). (C) The low-affinity library was incubated with 650 nM LRP6, and the purple rectangle represents clones that bind to LRP6.

The binding between Scl_{WT} or its variants to the immobilized LRP4 receptor was determined at 25 °C with HEPES-buffered saline (10 mM HEPES, 150 mM NaCl, 0.005% Tween) as the running buffer. Different concentrations of purified soluble proteins were allowed to flow over the chip at a flow rate of 30 $\mu L \cdot min^{-1}$ for 600 s, followed by dissociation for 600 s (for Scl_{WT}, Scl_{K75Q}, and Scl_{V136D}) or at a flow rate of 60 $\mu L \cdot min^{-1}$ for 200 s, followed by dissociation for 600 s (for Scl_{K75E}). The interactions obtained were normalized to the RU values of the BSA-immobilized channel. The dissociation constant (K_D) was determined using an equilibrium binding model.

Statistical analysis

Statistical analyses were performed with GRAPHPAD PRISM 8 (GraphPad Software, La Jolla, CA, USA). Data are presented as means ± SD. An unpaired, two-tailed Student's *t*-test was used to analyze between-group differences. Differences were considered significant at $P < 0.05$.

Results and Discussion

Identification of Scl positions critical for LRP4 binding

To identify Scl residues critical for the binding of Scl to LRP4, we utilized a YSD combinatorial library of Scl and soluble LRP4 as the target protein. We found that in the naïve library, 22% of the sequences contained a single mutation within the gene, with the remaining sequences containing 0, 2, or 3 mutations per clone. We then presorted the naïve library to eliminate the Scl variants with a stop codon or poor expression on the yeast surface and collected the library fraction with the highest expression levels (33% of the entire population) (Fig. 1A).

Thereafter, we sorted the high-expression library (termed the Scl_{NAIVE} library) for binding to 5 nM LRP4 (Fig. 1B) and collected cells with high expression and a low binding signal, that is, the fraction of variants that exhibited reduced binding affinity to LRP4 (termed the $LRP4_{LOW}$ library) (Fig. S1). Then, we resorted the $LRP4_{LOW}$ library for binding to 650 nM LRP6, a natural ligand for Scl, and collected all cells that exhibited binding to LRP6 (termed $LRP4_{LOW}$LRP6 library) (Fig. 1C). This screening step gave credence to our assumption that the reduced affinity for LRP4 could be attributed to a mutation specific to the LRP4-Scl binding interface, as these variants retained a certain degree of binding to LRP6. We were unable to screen the LRP4 low binders against LRP5 due to the unavailability of recombinant LRP5 protein, either commercial or in-house produced. Nevertheless, assuming that the binders pool would overlap is plausible since most of the LRP6 residues participating in Scl binding are conserved in LRP5 [21].

High-throughput sequencing analysis to identify Scl mutations that reduce affinity to LRP4

To identify Scl positions that directly interact with LRP4, the naïve and sorted libraries were sequenced using high-throughput sequencing and Illumina Miseq. Two overlapping amplicons (~300 base pairs) were required to cover the entire Scl gene (570 bp). The

total number of sequenced read pairs per library was 4 859 747 reads in the Scl_{NAIVE} library, 4 987 447 reads in the $LRP4_{LOW}$ library, and 3 571 408 reads in the $LRP4_{LOW}LRP6$ library. The reading frame required to translate each sequence into its respective amino acid sequence was selected using the Scl_{WT} sequence from UniProt (entry Q9BQB4) as a reference.

To remove short reads, reads with stop codons, or multiple mutations, reads were merged and filtered as follows. First, sequences that contained a premature stop codon (due to a mutation) or an incompletely specified nucleotide base (due to DNA sequencing errors) were filtered out (namely, 1 820 276, 1 866 731, and 1 560 446 in the Scl_{NAIVE}, $LRP4_{LOW}$, and $LRP4_{LOW}LRP6$ libraries, respectively). After the merging and filtering process, the remaining merged reads were 3 039 471 in the Scl_{NAIVE} library, 3 120 716 in the $LRP4_{LOW}$ library, and 2 010 962 in the $LRP4_{LOW}LRP6$ library. Of the total sequences subjected to quality filtering, 62.54%, 62.57%, and 56.31% of the sequences passed the quality filtering process in the Scl_{NAIVE}, $LRP4_{LOW}$, and $LRP4_{LOW}LRP6$ libraries, respectively.

On the premise that focusing solely on Scl single-mutation variants for further analysis would allow independent characterization of the contribution of each identified position to the LRP4 binding epitope of Scl, we proceeded as follows. We first filtered out the WT sequences and those containing multiple mutations; the final numbers of reads with a single mutation in the protein sequence were 140 338 in the Scl_{NAIVE} library, 141 861 in the $LRP4_{LOW}$ library, and 49 331 in the $LRP4_{LOW}LRP6$ library. Thereafter, we generated heat maps to enable the visualization of amino acid substitutions that resulted in statistically significant reduced affinity of Scl to LRP4, that is, hotspots (Fig. 2). In the $LRP4_{LOW}$ library fraction, we identified 20 potential hotspots (Fig. 2A and Table S1); in the $LRP4_{LOW}LRP6$ library fraction, we identified 42 LRP6 binders (Fig. 2B).

To select Scl variants for experimental validation of Scl positions that interact with LRP4 based on the $LRP4_{LOW}$ library heat map (Fig. 2A and Fig. S2), we classified the variants according to: (i) variants with mutations in loop 1, loop 3, or the N-terminal arm of Scl (Fig. 3, and Table S1, indicated on a green background); (ii) variants with mutations in positions identified from the $LRP4_{LOW}$ and $LRP4_{LOW}LRP6$ heat maps (Fig. 2C), namely, positions that interact directly with LRP4 without destabilizing the Scl structure; and (iii) variants with mutations in positions that are evolutionarily conserved in Scl, as such positions may be important for the interactions of Scl with LRP4 [45,46]. Positions located in the C-terminal arm or loop 2 of Scl were excluded, as those regions were shown to interact with LRP6 (Table S1, indicated on a white background) [20,21]. The positions adjacent to the cysteines that form the cystine knot structure of Scl (i.e., K143E, K145E, and K145R; Table S1, indicated on a yellow background) were not considered for experimental validation due to their possible destabilizing effect on the cystine knot structure of the protein. Thus, the following seven positions were selected for functional validation (Table 1): T11, K75, K135, and V136 [all meet criteria (i) and (ii)], E59 [meets criteria (i) and (iii)], and K135 and V136 [both meet criteria (i), (ii), and (iii)]. The locations of the positions in the Scl_{WT} structure are shown in Fig. 3.

Validation of the affinity change of Scl single-mutation variants to LRP4 by using YSD

To experimentally validate our selected single-mutation variants, we compared, using YSD, the binding of Scl_{WT} and its variants (Table 1) to soluble LRP4 at different concentrations. At an LRP4 concentration of 1 nM, most variants exhibited profoundly lower binding to LRP4 than Scl_{WT} (Fig. 4A). Moreover, Scl_{K75E}, Scl_{K135R}, and Scl_{V136D} displayed consistently lower binding to LRP4 at higher LRP4 concentrations (i.e., 10 and 50 nM; Fig. 4B,C). These results are in agreement with the high-throughput screening and analysis, as ~70% of the tested variants showed reduced binding affinity to LRP4 compared to Scl_{WT}.

Production and characterization of the selected Scl single-mutation variants

To further validate the high-throughput screening and analysis results, five Scl variants (i.e., Scl_{T11A}, Scl_{K75Q}, Scl_{K75E}, Scl_{K135R}, and Scl_{V136D}) that displayed reduced affinity to 1 nM LRP4 in the YSD setup were expressed in the *Pichia pastoris* GS115 yeast strain and purified using affinity chromatography. The Scl_{K135R} variant precipitated rapidly during the buffer exchange following Ni-NTA chromatography elution (data not shown). On SDS/PAGE, Scl_{T11A} migrated as a smeared band between 35 and 45 kDa, which is typical of glycosylated proteins due to the glycosylation heterogeneity [47]. The other purified recombinant proteins (i.e., Scl_{WT}, Scl_{K75Q}, Scl_{K75E}, and Scl_{V136D}) migrated with identical profiles, with a main band at ~32 kDa (Fig. 5). Given that there are two N-glycosylation sites in Scl_{WT} (based on the sequence analysis and experimental data [24,27,48,49]), it was

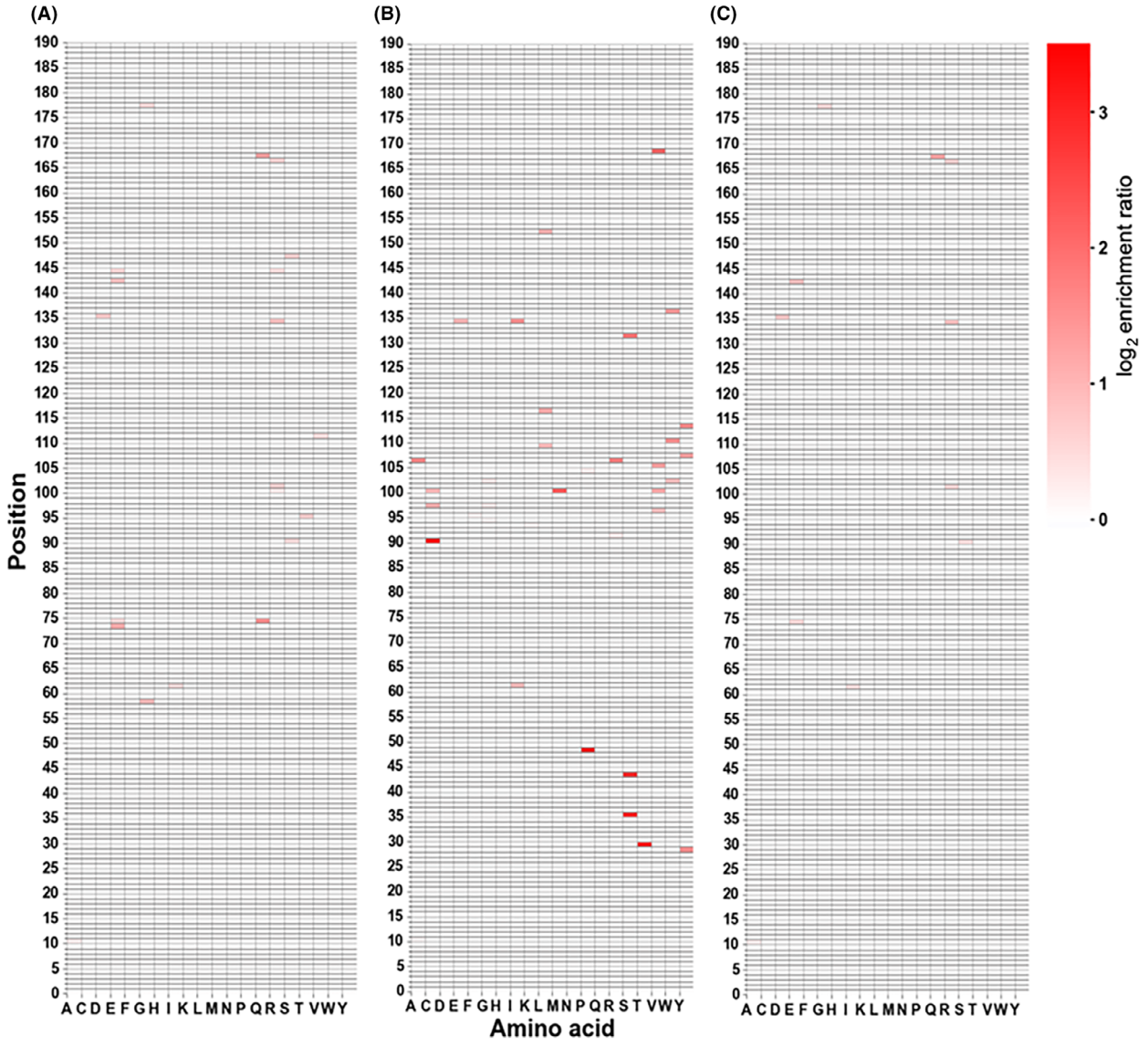

Fig. 2. Identification of affinity-reducing mutations. Heat maps demonstrating significantly enriched Scl variants in (A) $LRP4_{LOW}$ library compared to Scl_{NAIVE} library fractions; (B) $LRP4_{LOW}$LRP6 library compared to $LRP4_{LOW}$ library fractions; (C) $LRP4_{LOW}$ library compared to Scl_{NAIVE} library fractions that overlap with the $LRP4_{LOW}$LRP6 library. The heat maps present the log_2 transformation of the ER (red scale bar on the right-hand side) and highlight single mutations that significantly (A) reduce the binding affinity to LRP4, (B) reduce the binding affinity to LRP4 and retain binding to LRP6, and (C) overlap in (A) and (B). The substituting amino acids are shown on the *X*-axis, and the substituted positions are shown on the *Y*-axis. Statistical significance was determined by a two-sided Poisson exact test and multi-test corrected by the Benjamini–Hochberg FDR.

necessary to confirm that the SDS/PAGE migration pattern was a result of glycosylation. To this end, we treated a small fraction of each recombinant protein with Endo Hf endoglycosidase, which cleaves N-linked glycoproteins. After this treatment, the main band for all the proteins emerged at the expected size of ~ 27 kDa (Fig. 5), confirming the presence of glycosylation sites.

Since some of the mutations (i.e., K75E and V136D) encode for nonconserved amino acid substitutions [50,51] and may affect protein stability and conformation, it was also necessary to confirm that the affinity reduction to LRP4 was not due to the destabilizing effect of the amino acid substitutions on the Scl structure. Therefore, we examined the thermal stability of Scl_{WT} and its variants (i.e., Scl_{T11A}, Scl_{K75Q},

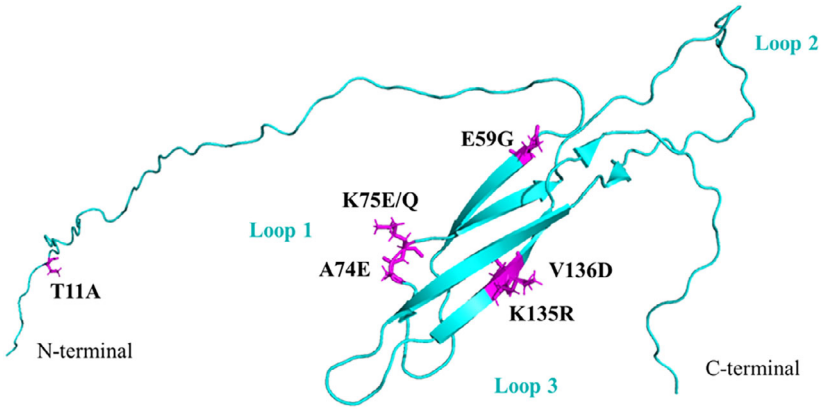

Fig. 3. Single-mutation variants selected for empirical validation depicted on the Scl_{WT} structure. Purple residues indicate positions with affinity-reducing mutations. The C-terminal region has been truncated for image clarity.

Table 1. Scl single-mutation variants selected for empirical validation by YSD.

Scl variant	No. of repeats in Scl_{NAIVE} library	No. of repeats in $LRP4_{LOW}$ library	log2 ER[a]	*P*-value[b]	Rank[c]	*P*-value adj[d]
T11A	1206	1444	0.272	$8.64{\cdot}10^{-05}$	26	$3.73{\cdot}10^{-03}$
E59G	258	479	0.905	$5.10{\cdot}10^{-15}$	2	$2.86{\cdot}10^{-12}$
A74E	34	73	1.115	$3.08{\cdot}10^{-04}$	31	$1.12{\cdot}10^{-02}$
K75E	202	289	0.529	$2.98{\cdot}10^{-04}$	30	$1.12{\cdot}10^{-02}$
K75Q	12	34	1.515	$1.71{\cdot}10^{-03}$	46	$4.17{\cdot}10^{-02}$
K135R	171	305	0.847	$4.76{\cdot}10^{-09}$	5	$1.07{\cdot}10^{-06}$
V136D	122	201	0.732	$3.56{\cdot}10^{-05}$	21	$1.90{\cdot}10^{-03}$

[a]Positive $\log_2$ ER values represent variants enriched in the sorted population; [b]*P*-value < 0.05 represents statistically significant variants based on a two-sided Poisson exact test; [c]Rank represents a ranking order assigned to the *P*-value, using the Benjamini–Hochberg procedure; [d]*P*-value adj represents the corrected significance value based on the multiple comparison testing.

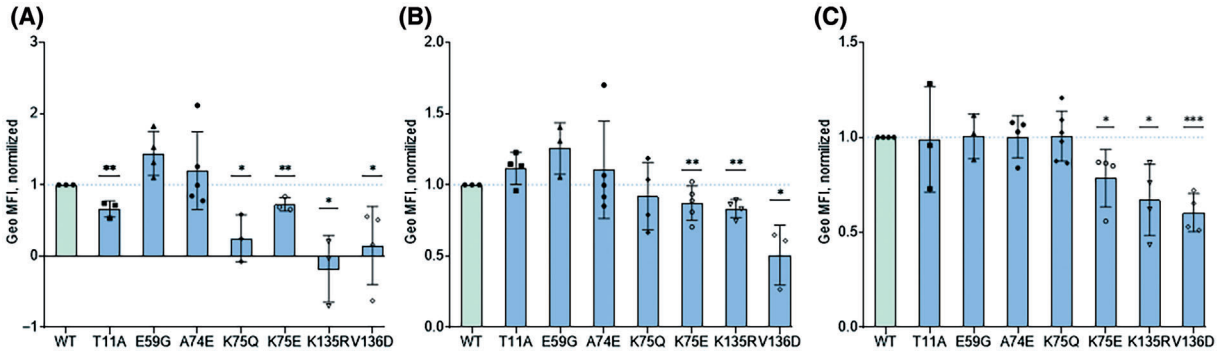

Fig. 4. YSD binding of Scl_{WT} and the selected single-mutation variants to LRP4. Geometric mean fluorescence intensity (Geo MFI) is presented as a fold change. Recombinant yeast cells expressing Scl_{WT} or its variants were incubated with (A) 1 nM, (B) 10 nM, or (C) 50 nM soluble LRP4. The binding signal of each Scl variant was normalized first to the expression signal of the corresponding variant and then to the binding signal of Scl_{WT} at the respective LRP4 concentration. Each experiment was repeated at least three times, and the results are presented as means ± SD. Statistical significance was assessed using an unpaired, two-tailed Student's *t*-test. $*P \leq 0.05$; $**P \leq 0.01$; $***P \leq 0.001$.

Scl_{K75E}, and Scl_{V136D}) by using DSC. The DSC signal for Scl_{WT} yielded two calorimetric peaks, one at 48.63 °C and the other at 50.55 °C (Fig. 6A and Table S2). The latter peak probably corresponds to the denaturation of the three disulfide bonds comprising the cystine knot fold of Scl_{WT}. The shape and area of the DSC traces for Scl_{K75Q}, Scl_{K75E}, and Scl_{V136D} were similar to those of Scl_{WT} (Fig. 6A). Moreover,

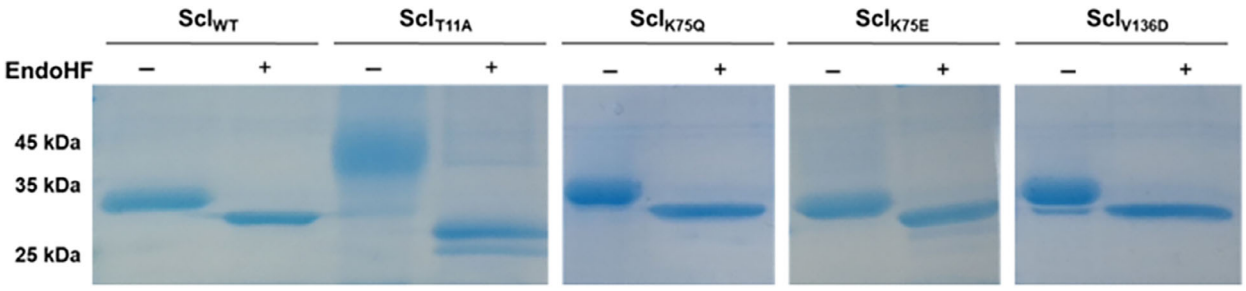

Fig. 5. Protein production and purification. SDS/PAGE analysis (reducing conditions) of Scl$_{WT}$ and Scl single-mutation variants expressed and purified in the *Pichia pastoris* GS115 strain before (–) and after (+) treatment with Endo Hf endoglycosidase for N-glycosylation cleavage.

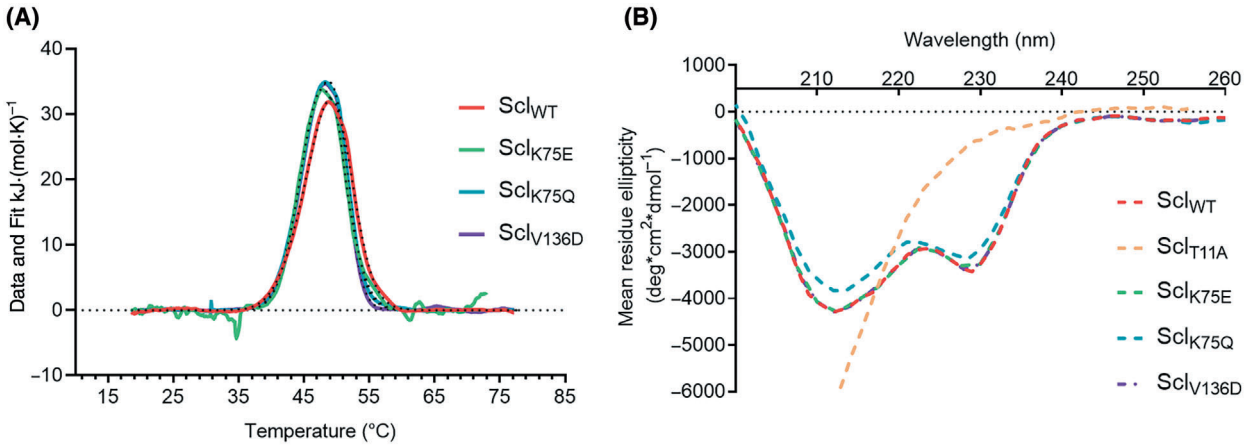

Fig. 6. DSC thermal profiles and CD spectra of purified Scl$_{WT}$ and Scl single-mutation variants. (A) All DSC thermal profiles were obtained in HEPES-buffered saline (10 mM HEPES, 150 mM NaCl), pH = 7.5, at a protein concentration of 0.5 mg·mL^{-1}. The experimental data are represented by solid lines with different colors for the different protein variants assayed. The dashed black lines represent the best fit to the Gaussian two-peak model. (B) All CD spectra were obtained at 25 °C at protein concentration of 0.2 mg·mL^{-1}.

the DSC parameters corresponding to Scl variants were close to the values derived from the thermogram of Scl$_{WT}$ (Table S2). This indicates that the tested proteins have similar thermodynamic properties and can be expected to have similar stability and folding kinetics. No DSC signal was obtained for Scl$_{T11A}$ (data not shown).

To evaluate whether the mutations affected the secondary structure of Scl, we compared the CD signal of three of the Scl variants (i.e., Scl$_{K75Q}$, Scl$_{K75E}$, and Scl$_{V136D}$) in the far UV region (200–260 nm) to the signal of Scl$_{WT}$. The absence of any significant difference in the overall shape of the spectral profiles between Scl$_{WT}$ and the three variants indicates that the secondary structure was unaffected by the mutations (Fig. 6B). The signal obtained for Scl$_{T11A}$ resembled the spectral form of an unfolded protein, which also explains the absence of a DSC peak for that variant.

Finally, we compared the binding of Scl$_{WT}$ and its variants (Scl$_{K75Q}$, Scl$_{K75E}$, and Scl$_{V136D}$) to LRP4 by using SPR. The assay was conducted with 3 (Fig. 7) or 6 µg (Fig. S3) of immobilized LRP4 receptor. The average K_D value of Scl$_{WT}$ was 2.18 µM, while Scl$_{K75Q}$ and Scl$_{K75E}$ showed, on average, more than a 10-fold reduction in affinity (K_D = 20.25 µM and K_D = 35.9 µM, respectively), and the affinity of Scl$_{V136D}$ to LRP4 decreased by 3.5-fold (average K_D = 7.52 µM) (Fig. 7). These results are consistent with our high-throughput screening and YSD empirical validation results. In addition, residues K75 (loop 1) and V136 (loop 3) in Scl are positioned in a hydrophobic patch formed by loops 1 and 3, which was previously suggested as a potential protein binding site [19], further supporting our assertion that these residues participate in LRP4–Scl binding.

Conclusions

To identify residues in Scl that are important for its binding to LRP4, we utilized a YSD-based epitope

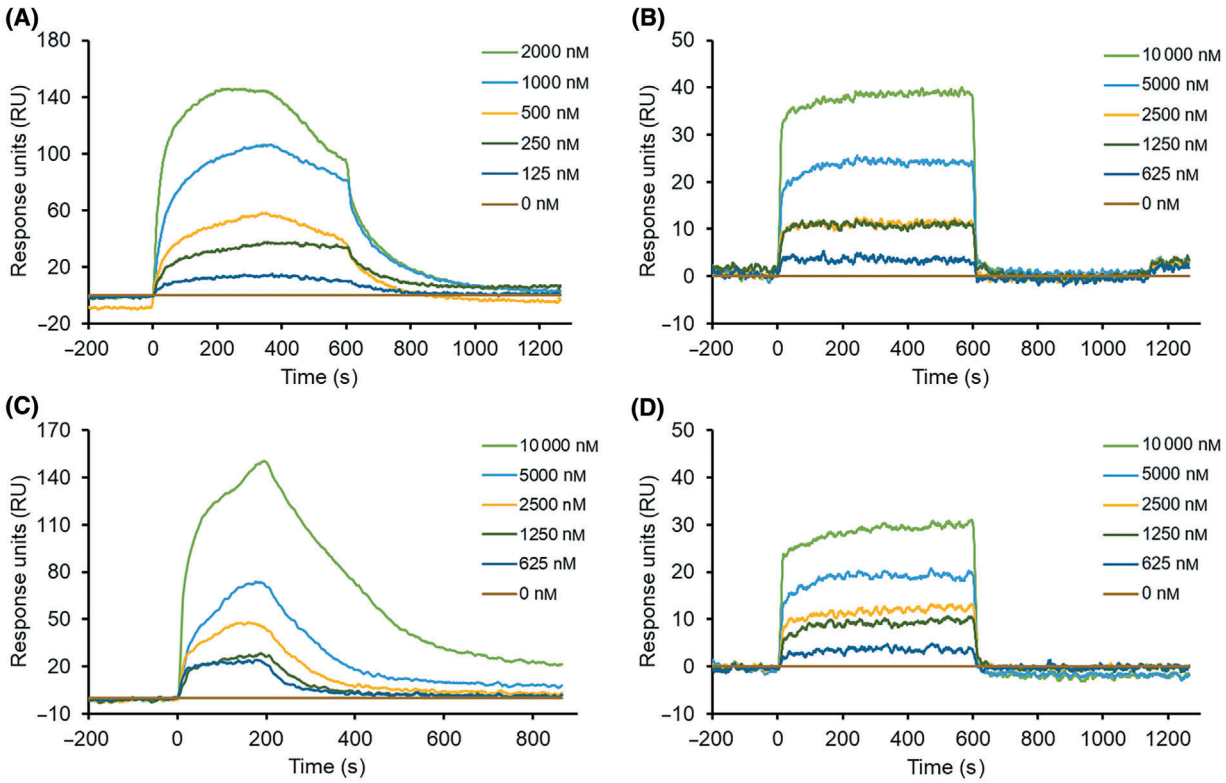

Fig. 7. SPR analysis of binding of purified Scl_{WT} and Scl single-mutation variants to LRP4. SPR data showing binding of (A) Scl_{WT}, (B) Scl_{K75Q}, (C) Scl_{K75E}, and (D) Scl_{V136D} to 3 µg of immobilized LRP4 receptor. Different protein concentrations are represented by different colors.

mapping approach combined with high-throughput sequencing and bioinformatic analysis. For this purpose, we screened a combinatorial library of Scl single-mutation variants for reduced binding to LRP4. This process generated seven residues in Scl that are potentially involved in the LRP4–Scl interaction based on high-throughput sequencing and computational analysis of the variants enriched in the screening process.

By experimental validation, we identified positions K75 (loop 1) and V136 (loop 3) in Scl as hotspots for the binding of Scl to LRP4. These positions are highly conserved in different species, further supporting their importance for protein interaction (Fig. S4). By revealing Scl positions critical to LRP4 interactions, we aid in the understanding of the Scl–LRP4 signaling mechanism and hence facilitate the development of target-specific therapeutic agents with the ability to sterically occlude the Scl-LRP4 binding interface. Further functional examination of the impact of amino acid substitution in these positions on the Wnt pathway *in vitro* and *in vivo* is needed, as our earlier research suggests that compounds that inhibit Scl–LRP4 interactions may promote bone formation [14].

In addition, we stress that our method can also be applied for the identification of crucial residues in other PPIs. Our approach is especially beneficial for protein complexes that, such as the human Scl–LRP4 complex, do not have solved structures or require laborious and time-consuming expression and purification protocols.

Acknowledgements

The authors thank Dr Alon Zilka and Dr Sofiya Kolusheva for their technical assistance. SPR experiments were performed at the NIBN Proteomics, Cytometry and Microscopy Unit, and DSC experiments were performed at the Research Support Laboratories of the Ilse Katz Institute for Nanoscale Science and Technology. Reut Meiri thanks the Israel Data Science and AI Initiative for providing cloud computing credit for this work. This work was supported by the National Institutes of Health (R01GM144393) to YO and NP, and the Rosetrees Trust (OoR2022/100004), the Israel Science Foundation (grant number 1615/19), and the Worldwide Cancer Research (grant number 20-0238) to NP.

Author contributions

SK is responsible for conceptualization, formal analysis, data curation, investigation, methodology, validation, visualization, writing—original draft, review and editing. RM is responsible for methodology, formal analysis, visualization, writing—original draft, review and editing. SL-H is responsible for Methodology. YO is responsible for formal analysis, funding acquisition, methodology, resources, supervision, validation, visualization, writing—original draft, writing—review and editing. NL is responsible for conceptualization, formal analysis, funding acquisition, investigation, methodology, resources, supervision, validation, visualization, writing—original draft, writing—review and editing. NP is responsible for conceptualization, formal analysis, funding acquisition, investigation, methodology, resources, supervision, validation, visualization, writing—original draft, writing—review and editing.

Peer review

The peer review history for this article is available at https://www.webofscience.com/api/gateway/wos/peer-review/10.1002/1873-3468.15033.

Data accessibility

Computational analysis code of the high-throughput sequencing data is publicly available at https://github.com/OrensteinLab/Sclerostin.

References

1 Boudin E, Fijalkowski I, Piters E and van Hul W (2013) The role of extracellular modulators of canonical Wnt signaling in bone metabolism and diseases. *Semin Arthritis Rheum* **43**, 220–240.

2 Krishnan V, Bryant HU and MacDougald OA (2006) Regulation of bone mass by Wnt signaling. *J Clin Invest* **116**, 1202–1209.

3 Dallas SL, Prideaux M and Bonewald LF (2013) The osteocyte: an endocrine cell … and more. *Endocr Rev* **34**, 658–690.

4 Winkler DG, Sutherland MK, Geoghegan JC, Yu C, Hayes T, Skonier JE, Shpektor D, Jonas M, Kovacevich BR, Staehling-Hampton K *et al.* (2003) Osteocyte control of bone formation via sclerostin, a novel BMP antagonist. *EMBO J* **22**, 6267–6276.

5 van Bezooijen RL, Svensson JP, Eefting D, Visser A, van der Horst G, Karperien M, Quax PHA, Vrieling H, Papapoulos SE, ten Dijke P *et al.* (2007) Wnt but not BMP signaling is involved in the inhibitory action of sclerostin on BMP-stimulated bone formation. *J Bone Miner Res* **22**, 19–28.

6 van Bezooijen RL, Roelen BAJ, Visser A, van der Wee-Pals L, de Wilt E, Karperien M, Hamersma H, Papapoulos SE, ten Dijke P and Löwik CWGM (2004) Sclerostin is an osteocyte-expressed negative regulator of bone formation, but not a classical BMP antagonist. *J Exp Med* **199**, 805–814.

7 Bullock WA, Hoggatt AM, Horan DJ, Elmendorf AJ, Sato AY, Bellido T, Loots GG, Pavalko FM and Robling AG (2019) Lrp4 mediates bone homeostasis and mechanotransduction through interaction with sclerostin in vivo. *iScience* **20**, 205–215.

8 Li X, Zhang Y, Kang H, Liu W, Liu P, Zhang J, Harris SE and Wu D (2005) Sclerostin binds to LRP5/6 and antagonizes canonical Wnt signaling. *J Biol Chem* **280**, 19883–19887.

9 Choi HY, Dieckmann M, Herz J and Niemeier A (2009) Lrp4, a novel receptor for dickkopf 1 and sclerostin, is expressed by osteoblasts and regulates bone growth and turnover in vivo. *PLoS One* **4**, e7930.

10 Fijalkowski I, Geets E, Steenackers E, van Hoof V, Ramos FJ, Mortier G, Fortuna AM, van Hul W and Boudin E (2016) A novel domain-specific mutation in a sclerosteosis patient suggests a role of LRP4 as an anchor for sclerostin in human bone. *J Bone Miner Res* **31**, 874–881.

11 Leupin O, Piters E, Halleux C, Hu S, Kramer I, Morvan F, Bouwmeester T, Schirle M, Bueno-Lozano M, Ramos Fuentes FJ *et al.* (2011) Bone overgrowth-associated mutations in the LRP4 gene impair sclerostin facilitator function. *J Biol Chem* **286**, 19489–19500.

12 Chang MK, Kramer I, Huber T, Kinzel B, Guth-Gundel S, Leupin O and Kneissel M (2014) Disruption of Lrp4 function by genetic deletion or pharmacological blockade increases bone mass and serum sclerostin levels. *Proc Natl Acad Sci USA* **111**, E5187–E5195.

13 Boudin E, Yorgan T, Fijalkowski I, Sonntag S, Steenackers E, Hendrickx G, Peeters S, de Maré A, Vervaet B, Verhulst A *et al.* (2017) The Lrp4R1170Q homozygous Knock-in mouse recapitulates the bone phenotype of sclerosteosis in humans. *J Bone Miner Res* **32**, 1739–1749.

14 Katchkovsky S, Chatterjee B, Abramovitch-Dahan C-V, Papo N and Levaot N (2022) Competitive blocking of LRP4–sclerostin binding interface strongly promotes bone anabolic functions. *Cell Mol Life Sci* **79**, 113.

15 Strickland DK, Gonias SL and Argraves WS (2002) Diverse roles for the LDL receptor family. *Trends Endocrinol Metab* **13**, 66–74.

16 He X, Semenov M, Tamai K and Zeng X (2004) LDL receptor-related proteins 5 and 6 in Wnt/β-catenin signaling:arrows point the way. *Development* **131**, 1663–1677.

17 MacDonald BT, Tamai K and He X (2009) Wnt/β-catenin signaling: components, mechanisms, and diseases. *Dev Cell* **17**, 9–26.
18 Johnson EB, Hammer RE and Herz J (2005) Abnormal development of the apical ectodermal ridge and polysyndactyly in Megf7-deficient mice. *Hum Mol Genet* **14**, 3523–3538.
19 Veverka V, Henry AJ, Slocombe PM, Ventom A, Mulloy B, Muskett FW, Muzylak M, Greenslade K, Moore A, Zhang L *et al.* (2009) Characterization of the structural features and interactions of sclerostin. Molecular insight into a key regulator of Wnt-mediated bone formation. *J Biol Chem* **284**, 10890–10900.
20 Bourhis E, Wang W, Tam C, Hwang J, Zhang Y, Spittler D, Huang OW, Gong Y, Estevez A, Zilberleyb I *et al.* (2011) Wnt antagonists bind through a short peptide to the first β-propeller domain of LRP5/6. *Structure* **19**, 1433–1442.
21 Kim J, Han W, Park T, Kim EJ, Bang I, Lee HS, Jeong Y, Roh K, Kim J, Kim JS *et al.* (2020) Sclerostin inhibits Wnt signaling through tandem interaction with two LRP6 ectodomains. *Nat Commun* **11**, 5357.
22 Boschert V, van Dinther M, Weidauer S, van Pee K, Muth EM, Ten Dijke P and Mueller TD (2013) Mutational analysis of sclerostin shows importance of the flexible loop and the cystine-knot for Wnt-signaling inhibition. *PLoS One* **8**, e81710.
23 Holdsworth G, Slocombe P, Doyle C, Sweeney B, Veverka V, le Riche K, Franklin RJ, Compson J, Brookings D, Turner J *et al.* (2012) Characterization of the interaction of sclerostin with the low density lipoprotein receptor-related protein (LRP) family of wnt co-receptors. *J Biol Chem* **287**, 26464–26477.
24 Balemans W, Ebeling M, Patel N, van Hul E, Olson P, Dioszegi M, Lacza C, Wuyts W, van den Ende J, Willems P *et al.* (2001) Increased bone density in sclerosteosis is due to the deficiency of a novel secreted protein (SOST). *Hum Mol Genet* **10**, 537–544.
25 Balemans W, Patel N, Ebeling M, van Hul E, Wuyts W, Lacza C, Dioszegi M, Dikkers FG, Hildering P, Willems PJ *et al.* (2002) Identification of a 52 kb deletion downstream of the SOST gene in patients with van Buchem disease. *J Med Genet* **39**, 91–97.
26 Staehling-Hampton K, Proll S, Paeper BW, Zhao L, Charmley P, Brown A, Gardner JC, Galas D, Schatzman RC, Beighton P *et al.* (2002) A 52-kb deletion in the SOST-MEOX1 intergenic region on 17q12-q21 is associated with van Buchem disease in the Dutch population. *Am J Med Genet* **110**, 144–152.
27 Brunkow ME, Gardner JC, Van Ness J, Paeper BW, Kovacevich BR, Proll S, Skonier JE, Zhao L, Sabo PJ, Fu Y *et al.* (2001) Bone dysplasia sclerosteosis results from loss of the SOST gene product, a novel cystine knot-containing protein. *Am J Hum Genet* **68**, 577–589.
28 Whyte MP, Deepak Amalnath S, McAlister WH, Pedapati R, Muthupillai V, Duan S, Huskey M, Bijanki VN and Mumm S (2018) Sclerosteosis: report of type 1 or 2 in three Indian Tamil families and literature review. *Bone* **116**, 321–332.
29 Huybrechts Y, Boudin E, Hendrickx G, Steenackers E, Hamdy N, Mortier G, Martínez Díaz-Guerra G, Bracamonte MS, Appelman-Dijkstra NM and Van Hul W (2022) Identification of compound heterozygous variants in LRP4 demonstrates that a pathogenic variant outside the third β-propeller domain can cause sclerosteosis. *Genes (Basel)* **13**, 80.
30 Kim N, Stiegler AL, Cameron TO, Hallock PT, Gomez AM, Huang JH, Hubbard SR, Dustin ML and Burden SJ (2008) Lrp4 is a receptor for Agrin and forms a complex with MuSK. *Cell* **135**, 334–342.
31 Weiss GA, Watanabe CK, Zhong A, Goddard A and Sidhu SS (2000) Rapid mapping of protein functional epitopes by combinatorial alanine scanning. *Proc Natl Acad Sci USA* **97**, 8950–8954.
32 Ramos RM and Moreira IS (2013) Computational alanine scanning mutagenesis—an improved methodological approach for protein–DNA complexes. *J Chem Theory Comput* **9**, 4243–4256.
33 Boder ET and Wittrup KD (1997) Yeast surface display for screening combinatorial polypeptide libraries. *Nat Biotechnol* **15**, 553–557.
34 VanAntwerp JJ and Wittrup KD (2000) Fine affinity discrimination by yeast surface display and flow cytometry. *Biotechnol Prog* **16**, 31–37.
35 Chao G, Lau WL, Hackel BJ, Sazinsky SL, Lippow SM and Wittrup KD (2006) Isolating and engineering human antibodies using yeast surface display. *Nat Protoc* **1**, 755–768.
36 Naftaly S, Cohen I, Shahar A, Hockla A, Radisky ES and Papo N (2018) Mapping protein selectivity landscapes using multi-target selective screening and next-generation sequencing of combinatorial libraries. *Nat Commun* **9**, 1–10.
37 Aharon L, Aharoni S-L, Radisky ES and Papo N (2020) Quantitative mapping of binding specificity landscapes for homologous targets by using a high-throughput method. *Biochem J* **477**, 1701–1719.
38 Whitehead TA, Chevalier A, Song Y, Dreyfus C, Fleishman SJ, de Mattos C, Myers CA, Kamisetty H, Blair P, Wilson IA *et al.* (2012) Optimization of affinity, specificity and function of designed influenza inhibitors using deep sequencing. *Nat Biotechnol* **30**, 543–548.
39 Bass SH, Mulkerrin MG and Wells JA (1991) A systematic mutational analysis of hormone-binding determinants in the human growth hormone receptor. *Proc Natl Acad Sci USA* **88**, 4498–4502.
40 DeLano WL (2002) Unraveling hot spots in binding interfaces: progress and challenges. *Curr Opin Struct Biol* **12**, 14–20.

41 Bateman A, Martin MJ, Orchard S, Magrane M, Ahmad S, Alpi E, Bowler-Barnett EH, Britto R, Bye-A-Jee H, Cukura A *et al.* (2023) UniProt: the universal protein knowledgebase in 2023. *Nucleic Acids Res* **51**, D523–D531.
42 Fowler DM, Araya CL, Gerard W and Fields S (2011) Enrich: software for analysis of protein function by enrichment and depletion of variants. *Bioinformatics* **27**, 3430–3431.
43 Storey JD and Tibshirani R (2003) Statistical significance for genomewide studies. *Proc Natl Acad Sci USA* **100**, 9440–9445.
44 Rosenfeld L, Shirian J, Zur Y, Levaot N, Shifman JM and Papo N (2015) Combinatorial and computational approaches to identify interactions of macrophage colony-stimulating factor (M-CSF) and its receptor c-FMS. *J Biol Chem* **290**, 26180–26193.
45 Ma B, Elkayam T, Wolfson H and Nussinov R (2003) Protein-protein interactions: structurally conserved residues distinguish between binding sites and exposed protein surfaces. *Proc Natl Acad Sci USA* **100**, 5772–5777.
46 Guharoy M and Chakrabarti P (2010) Conserved residue clusters at protein-protein interfaces and their use in binding site identification. *BMC Bioinformatics* **11**, 1–17.
47 Gemmill TR and Trimble RB (1999) Overview of N- and O-linked oligosaccharide structures found in various yeast species. *Biochim Biophys Acta Gen Subj* **1426**, 227–237.
48 Kusu N, Laurikkala J, Imanishi M, Usui H, Konishi M, Miyake A, Thesleff I and Itoh N (2003) Sclerostin is a novel secreted osteoclast-derived bone morphogenetic protein antagonist with unique ligand specificity. **278**, 24113–24117.
49 Krause C, Korchynskyi O, de Rooij K, Weidauer SE, de Gorter DJ, van Bezooijen RL, Hatsell S, Economides AN, Mueller TD, Löwik CW *et al.* (2010) Distinct modes of inhibition by sclerostin on bone morphogenetic protein and Wnt signaling pathways. *J Biol Chem* **285**, 41614–41626.
50 Gray VE, Hause RJ and Fowler DM (2017) Analysis of large-scale mutagenesis data to assess the impact of single amino acid substitutions. *Genetics* **207**, 53–61.
51 Betts MJ and Russell RB (2007) Amino-acid properties and consequences of substitutions. In Bioinformatics for Geneticists (Barnes MR and Gray IC, eds), pp. 311–342. Wiley, Hoboken, NJ.

Supporting information

Additional supporting information may be found online in the Supporting Information section at the end of the article.

Fig. S1. Contour plot illustrating the superposition of binding to LRP4 analysis of Scl_{NAIVE} (black) and $LRP4_{LOW}$ (magenta) libraries.

Fig. S2. Identification of affinity-reducing mutations.

Fig. S3. SPR analysis of binding of purified Scl_{WT} and Scl single-mutation variants to LRP4.

Fig. S4. Sequence alignment to show positions in Scl that are highly conserved in different species.

Table S1. Identified Scl single-mutation variants[a] with decreased binding to LRP4.

Table S2. Thermodynamic parameters of the thermal unfolding of different Scl variants obtained from the analysis of differential scanning calorimetry experiments.